

# Instability analysis under part-load conditions in centrifugal pump<sup>†</sup>

Weixiang Ye<sup>1</sup>, Renfang Huang<sup>2</sup>, Zhiwu Jiang<sup>3</sup>, Xiaojun Li<sup>3</sup>, Zuchao Zhu<sup>3</sup> and Xianwu Luo<sup>1,\*</sup>

<sup>1</sup>State Key Laboratory of Hydrosience and Engineering, Department of Energy and Power Engineering, Tsinghua University, Beijing 100084, China

<sup>2</sup>Key Laboratory for Mechanics in Fluid Solid Coupling System, Institute of Mechanics, Chinese Academy of Sciences, Beijing 100190, China

<sup>3</sup>Key Laboratory of Fluid Transmission Technology of Zhejiang Province, Zhejiang Sci-Tech University, Hangzhou 310018, China

(Manuscript Received March 2, 2018; Revised July 29, 2018; Accepted August 5, 2018)

## Abstract

In this study, a centrifugal pump with a specific speed of  $39.12 \text{ m} \cdot \text{min}^{-1} \cdot \text{m}^3 \cdot \text{s}^{-1}$  is treated to analyze the flow instability under part-load conditions by numerical simulation and experimental test. For calculations, the RANS method, coupled with the  $k-\omega$  SST turbulence model, is adopted. Numerical results at different operation points are compared with available experimental data, such as hydraulic performance and flow field information by particle image velocimetry. The numerical and experiment results agree well. The flow simulation indicates a strong reverse flow at the passage upstream impeller inlet, and the energy loss in the impeller is the largest under part-load conditions among all flow components in the pump. In one impeller revolution, one blade-to-blade flow passage is always nearly blocked off by the rotating stall occurring at the impeller inlet for each instant, and the blockage induces a jet flow with large velocity at the next blade-to-blade flow passage along the rotational direction of the impeller. The blockage and the jet flow in the blade-to-blade flow passages will make the flow unstable inside the impeller and cause performance breakdown and pressure vibration under part-load conditions for the pump.

**Keywords:** Centrifugal pump; Flow instability; Part-load conditions; Rotating stall

## 1. Introduction

Flow instability is a common unsteady phenomenon in the field of hydraulic machinery that often causes violent pressure fluctuations and strong noise as units run under part-load conditions [1]. Avoiding the flow instability phenomenon as a pump runs under such conditions, i.e., high-head and small-flow conditions, is usually difficult [2, 3]. Fig. 1 compares hydraulic performance curves at different conditions. For general cases, only one intersection exists between the head performance curve of the pump and the characteristic curve of the pipeline, and the pump is operated under stable conditions. However, when two or more intersections exist between those two curves, a special physical phenomenon at part-load operations called “hump” occurs. The operating point is not fixed and can move back and forth between these intersections, and the pump is in a state of instability. Therefore, during the operation of the pump, especially a low-specific-speed centrifugal pump, the flow instability phenomenon must be suppressed as units run under part-load conditions.

To extensively investigate the flow instability phenomenon at part-load conditions, many studies have been conducted.

Ran et al. [4] considered that the hump region generally occurs at conditions of  $0.5Q_d \sim 0.6Q_d$  in the ordinary pump, where  $Q_d$  is the flow rate of the design point, whereas the hump region can be up to  $0.9Q_d$  in the pump turbine at pump mode. Mou et al. [5] believed that the appropriate number of blades, blade angle, and blade width at impeller exit would have a positive effect on the suppression of the flow instability phenomenon. Braun [6] investigated part-load flow in radial centrifugal pumps under off-design conditions by experimental and numerical methods and considered that adverse pressure gradients in the pump diffuser and secondary flow between guide vanes may cause flow separation, which may cause flow instability further. Some researchers have considered the phenomenon of flow separation [7, 8], recirculation at pump inlet passage [9–11], and rotating stall [12–15], which are associated with small-flow-rate conditions. All these phenomena would cause great energy loss, which may be the reason for the formation of flow instability.

The internal flow of a pump is analyzed through two main methods, namely, visualization experiment and numerical simulation. In an experiment, Ciocan et al. [16] performed the velocity distribution in the guide vanes of a pump turbine at hump conditions by using particle image velocimetry (PIV) and laser Doppler velocimetry, and presented the interaction between the generation of vortices in guide vanes and the

\*Corresponding author. Tel.: +86 10 62789853, Fax.: +86 10 62782508

E-mail address: [luoxw@tsinghua.edu.cn](mailto:luoxw@tsinghua.edu.cn)

<sup>†</sup> Recommended by Associate Editor Weon Gyu Shin

© KSME & Springer 2019

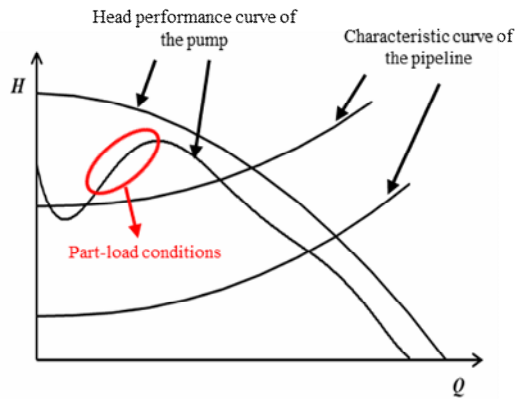


Fig. 1. Comparison of normal performance curve and performance curve at part-load conditions.

hump phenomenon. Meanwhile, with the development of computer technology and computational fluid dynamics (CFD), different numerical simulation methods, such as Reynolds-averaged Navier–Stokes (RANS) [17], large-eddy simulation [18, 19], and direct numerical simulation (DNS) [20] can be conducted to analyze complex flows at special operations in pumps. These results and improvements are helpful in revealing the mechanism of flow instability phenomenon.

In this work, a centrifugal pump with low specific speed is treated to study the flow instability phenomenon by using steady and unsteady flow simulation. The calculated results are compared with experimental results to preliminarily explore the instability of the flow in a centrifugal pump at part-load conditions and explain the mechanism of the rotating stall.

## 2. Test pump and simulation model

### 2.1 Geometry of centrifugal pump

The investigated pump has a specific speed of  $39.12 \text{ m} \cdot \text{min}^{-1} \cdot \text{m}^3 \cdot \text{s}^{-1}$ . The pump has a shrouded centrifugal impeller, which is shown in Fig. 2. At the designed operation condition, the flow rate is  $Q_d = 1.80 \text{ m}^3/\text{h}$ , the head is  $H_d = 2.67 \text{ m}$ , and the rotational speed is  $n = 1000 \text{ r/min}$ . The main details about the impeller are shown in Table 1.

For convenience of flow measurement by PIV, the front shroud and all the blades of the impeller are made of transparent Plexiglas, and the suction pipe is replaced by a special suction passage. The special suction passage has an inlet pipe, which is set beside the pump as shown in Fig. 3. To produce the same physical condition between the numerical simulation and the experimental test, two planes for pressure measurement are selected as the inlet and outlet, respectively, of the simulated model. Fig. 3 shows the test pump and the pressure measurement devices in the experiment. The computation domain for the pump is shown in Fig. 4. The simulation model includes an inlet pipe, impeller, and casing and outlet pipe, among others. For better convergence, an extension pipe is connected with the outlet pipe. Due to a large axial clearance between the pump cover and impeller shroud, a gap zone is

Table 1. Main geometrical parameters of pump impeller.

Parameter	Value
Impeller inlet diameter $D_1/\text{mm}$	56
Impeller exit diameter $D_2/\text{mm}$	142
Blade width at impeller exit $b_2/\text{mm}$	7
Blade number $Z$	5
Inlet angle of blade $\beta_1/^\circ$	19
Exit angle of blade $\beta_2/^\circ$	42
Wrap angle of blade $\varphi/^\circ$	106

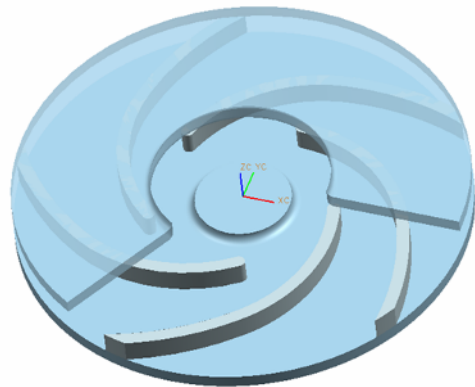


Fig. 2. Geometry of pump impeller.



Fig. 3. Test rig for experiments.

formed in the computation domain.

### 2.2 Mesh generation

In this work, structural mesh is generated for all flow components. Detailed meshes for different parts of the simulation

model are shown in Fig. 5. The mesh is provided suitable refinement near the blade wall.

Five sets of mesh with different numbers are selected for a mesh independence test, and the relative pump head  $H/H_d$  is used for comparison. As shown in Table 2, the mesh independence test indicates that a mesh of 3.2 million grid points is the acceptable compromise between the solution accuracy

Table 2. Mesh independence test.

	Mesh number	$H/H_d$
Mesh 1	1390176	0.963
Mesh 2	1926319	0.960
Mesh 3	2591883	1.014
Mesh 4	3203889	0.976
Mesh 5	3524505	0.974

Table 3.  $y^+$  distribution near wall surface at four operation conditions.

$Q/Q_d$	Blade	Hub and shroud
0.45	2.69~111.74	2.52~168.88
0.6	1.94~118.06	2.75~187.09
0.8	2.64~113.91	2.64~182.27
1.0	4.31~104.80	6.10~196.58

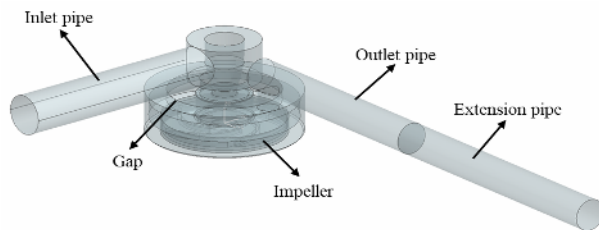


Fig. 4. Computation domain of pump.

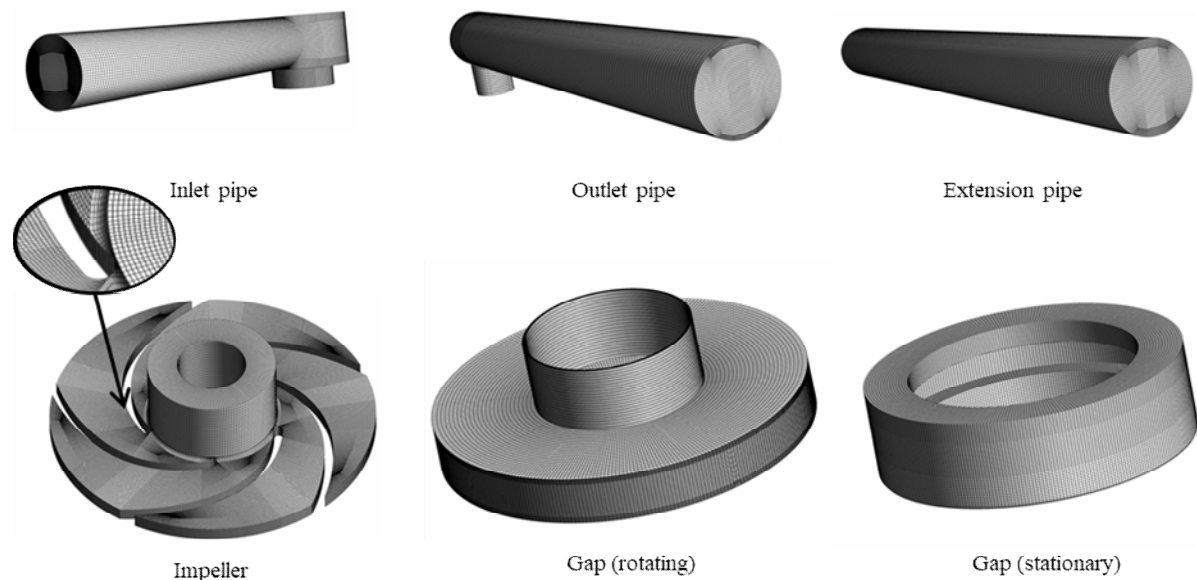


Fig. 5. Mesh generation for each flow component of computation domain.

requirement and the computer resources.

The  $y^+$  distribution near the wall surface in the computation domain under four conditions is shown in Table 3. The largest value of  $y^+$  is below 200, which meets the requirement of the wall function using the  $k-\omega$  SST turbulence model.

### 3. Numerical methods

Steady and unsteady simulations are conducted on the basis of RANS equations. The  $k-\omega$  SST turbulence model is used to capture the unstable behaviors, such as rotating stall and flow separation, at part-load conditions in the pump.

Water at 25 °C is selected as flow medium. A rotational coordinate system is set for the area of the pump impeller and the gap, and a stationary system is set for these stationary components. Interfaces exist between these connecting faces for two reference systems, where the sliding mesh strategy is applied. The boundary conditions are as follows. The mass flow rate according to the operation point is assigned at the domain inlet, and the total pressure is assigned at the domain outlet. All solid walls have non-slip boundary conditions.

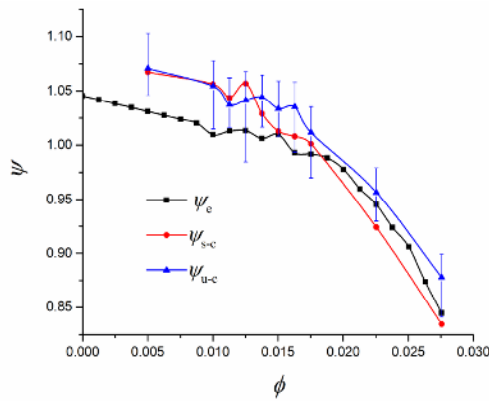
In the steady calculation, the residuals are set to  $1.0 \times 10^{-4}$ . For unsteady simulation, the time-dependent governing equations are discretized in space and in time. The time step is set as 0.001 s at first, corresponding to a runner-rotating angle of 6° per time step. After several revolutions, the time step is set as 0.0005 s, i.e., 3° per time step for the subsequent simulation. The residuals are set to  $1.0 \times 10^{-5}$ .

Numerical simulation is performed by using CFD commercial code ANSYS CFX 15.0.

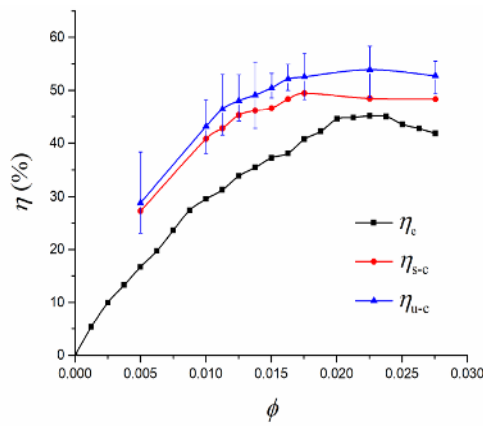
### 4. Results and analyses

#### 4.1 Characteristic curves

To show the pump performance, the non-dimensional pa-



(a)



(b)

Fig. 6. Characteristic curves of test pump.

rameters, flow coefficient  $\phi$  and head coefficient  $\psi$  [21] are defined as

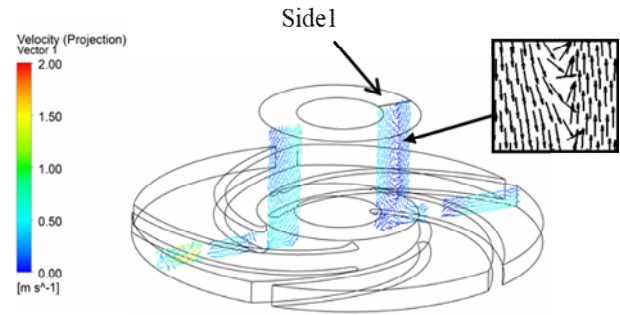
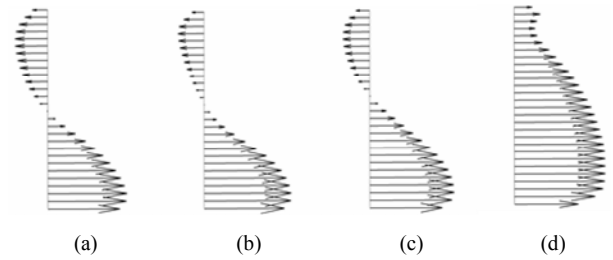
$$\phi = \frac{Q}{A_2 u_2}, \quad (1)$$

$$\psi = \frac{H}{u_2^2 / (2g)}, \quad (2)$$

where  $Q$  is the mass flow rate and  $A_2$  and  $u_2$  are the area and peripheral velocity at impeller exit, respectively.  $A_2$  can be calculated by  $A_2 = \pi D_2 b_2$ .

The characteristic curves of the test pump operated at  $n = 1000$  r/min are shown in Fig. 6, where the relation between head coefficient and flow coefficient (Fig. 6(a)), and that between efficiency and flow coefficient (Fig. 6(b)) are expressed. The subscript “e” means data by experiment, and the subscript “c” means data by calculation. For the numerical results, the subscript “s-c” represents results obtained by steady calculation, and the subscript “u-c” represents results obtained by unsteady simulation.

The pump has an unstable head when operated at a flow coefficient ranging from  $\phi = 0.008$  to  $\phi = 0.018$ , and the present simulation can reproduce the flow instability phenomenon in the pump. The results in Fig. 6 indicate that the pump head is

Fig. 7. Axial velocity distribution at inlet tube section,  $\phi = 0.0113$ .Fig. 8. Axial velocity distribution on centerline of inlet tube section at (a)  $\phi = 0.0113$ ; (b)  $\phi = 0.0125$ ; (c)  $\phi = 0.0175$ ; (d)  $\phi = 0.0225$ .

predicted well, and a discrepancy of efficiency is observed between the numerical and experimental data. This discrepancy is due to mechanical loss, which is not included in the numerical simulation.

The unsteady simulation predicts better performance tendency compared with the steady simulation. For the prediction of head coefficient, the steady simulation overestimates the pump head compared with experimental data at a flow coefficient below 0.018 and underestimates the pump head at a flow coefficient over 0.018. Meanwhile, the unsteady simulation always overestimates the pump head compared with the experiment. At the part-load conditions of  $\phi = 0.5\phi_{\text{bep}} \sim 0.6\phi_{\text{bep}}$  and  $\phi = 0.65\phi_{\text{bep}} \sim 0.72\phi_{\text{bep}}$ , the discrepancy is large, which indicates flow instability under such conditions. In addition, the prediction accuracy is fairly well around the design condition, i.e.,  $\phi_d = 0.0225$ , corresponding with  $Q_d = 1.8 \text{ m}^3/\text{h}$ . Furthermore, the best efficiency point is nearly the same as the design point, i.e.,  $\phi_{\text{bep}} = \phi_d$ .

The vertical bar in Fig. 6 represents the oscillation over the averaged head coefficient for the unsteady simulation. The head oscillations are larger at part-load conditions.

#### 4.2 Flow upstream impeller

To depict the flow inside the pump at different operation conditions, Figs. 7 and 8 show the velocity vector at one section of the impeller inlet cut along the pump shaft centerline, and the axial velocity distribution along a line (marked side 1 in Fig. 7) at different operation conditions.

At the operation condition of  $\phi = 0.0113$ , reverse flow is observed near the wall of the pump cover, and the reverse



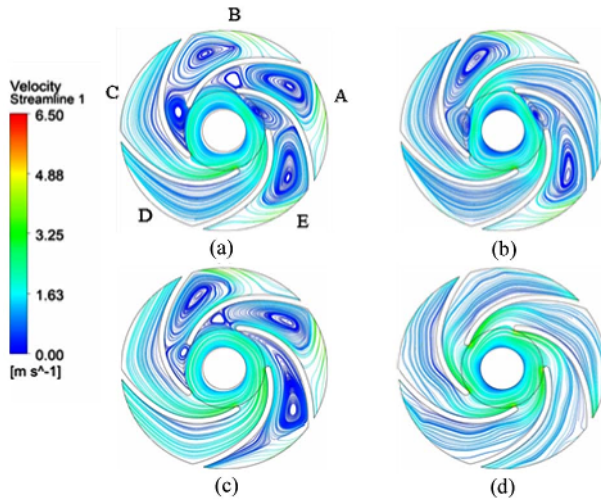


Fig. 9. Streamlines at mid-span section of impeller at (a)  $\phi = 0.0113$ ; (b)  $\phi = 0.0125$ ; (c)  $\phi = 0.0175$ ; (d)  $\phi = 0.0275$ .

flow occupies a sizable area of the flow passage. As the flow coefficient increases, the ratio of the reverse flow decreases. Though the axial velocity is not identical along the line, no reverse flow is seen at the design point, i.e.,  $\phi = \phi_d = 0.0225$ .

The reverse flow and vortices will result in energy loss in the flow passage of the impeller inlet. Thus, the operation points of three flow coefficients are located inside the region with flow instability. The operation condition of  $\phi = 0.0113$  is the left end of the region with flow instability, as shown in Fig. 6(a). Thus, the vortices may develop as the flow enters the impeller, and contribute to the flow instability phenomenon.

#### 4.3 Averaged flow in impeller

In Fig. 9, the averaged flows on the mid-span section of the impeller are presented at different operation conditions. For convenience of description, the passage near the pump outlet tube is named A, and other blade-to-blade passages are marked B to E, according to the rotation direction of the impeller.

At  $\phi = 0.0275$ , the streamlines on the mid-span section of the impeller are generally smooth, and no vortices are generated at the blade-to-blade passages. With a decrease in flow coefficient, vortices seem to develop in the impeller. Interestingly, two blade-to-blade flow passages are blocked off by the vortices at  $\phi = 0.0125$ , whereas three blade-to-blade flow passages are blocked off at  $\phi = 0.0175$  and  $\phi = 0.0113$ . These results indicate the vortices are not fixed in certain passages at different part-load conditions.

#### 4.4 Hydraulic loss

The impeller inlets have reverse flow, and the blade-to-blade passages have vortices. These unfavorable flows may cause hydraulic loss in the pump. The pump has a special flow passage downstream the impeller, and the inlet and outlet of

Table 4.  $CP$  in different flow components.

$\phi$	Inlet pipe	Impeller	Casing+gap	Outlet pipe
0.0050	-9.58	-246.78	-94.49	-24.73
0.0113	-3.19	-413.56	-36.11	-11.36
0.0125	-1.25	-267.44	-24.12	-10.63
0.0138	-5.21	-104.81	-24.26	-9.72
0.0150	-1.30	-45.22	-13.43	-12.67
0.0163	-1.26	-27.16	-16.58	-7.89
0.0175	-1.77	-58.61	-17.12	-6.93
0.0225	-0.47	-19.18	-11.54	-6.91
0.0276	-0.58	-15.83	-8.29	-7.55

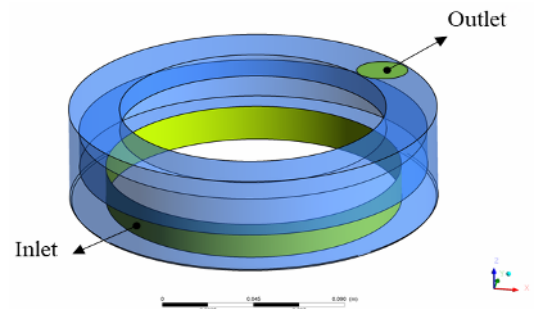


Fig. 10. Location definition for pump casing.

the pump casing are defined and shown in Fig. 10. The inlet is a cylindrical surface, and the outlet is a circular plane and connected with the outlet pipe of the test pump. The energy loss in each flow component is calculated at different flow conditions. The non-dimensional energy loss parameter, i.e.,  $CP$ , is defined as Eq. (3). Table 4 lists the results, wherein the energy loss in the pump impeller is the largest. Fig. 11 shows the non-dimensional energy loss parameter in the impeller at several operation conditions.

$$CP = \frac{p_{\text{outlet}} - p_{\text{inlet}}}{\rho \left( \frac{Q}{\pi D^2/4} \right)^2} - \frac{P_{\text{input}}}{Q \left( \frac{Q}{\pi D^2/4} \right)^2}, \quad (3)$$

where  $p_{\text{outlet}}$  and  $p_{\text{inlet}}$  are the total pressure at the inlet and outlet for each flow component, respectively.  $P_{\text{input}}$  represents the power input to the impeller, and  $D$  stands for the hydraulic diameter of each flow component.

The  $P_{\text{input}}$  value is positive for the impeller and zero for all stationary flow components. The results obtained in Table 4 and Fig. 11 indicate that the main energy loss occurs in the impeller and the casing. The circular outline and the outlet with a small section area contribute to hydraulic loss in the casing. The energy loss in the impeller is the largest among the flow components due to the presence of the vortices. At  $\phi = 0.0113$ , a peak with very large energy loss is observed due to the remarkable hydraulic loss in the pump operated near the flow instability conditions mentioned above.

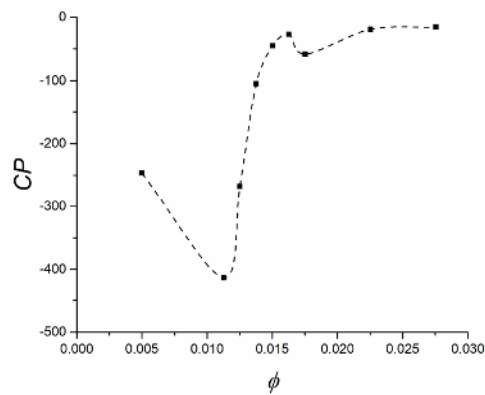


Fig. 11. Non-dimensional energy loss parameter of impeller at different operating conditions.

#### 4.5 Rotating stall

As the flow rate decreases from the design point, rotating stall will occur in the pump impeller, and the type of stall cells changes with the blade number. If the blade number is even, the alternative stall phenomenon will occur in the impeller of a centrifugal pump. If the blade number is odd, rotating stall occurs. The phenomenon of rotating stall can induce a head drop over the performance curve [22].

##### 4.5.1 Comparison between numerical simulation and PIV experiment

Three representative conditions with different flow rates are presented for unsteady analysis ( $\phi = 0.6\phi_{\text{bep}}$ ,  $\phi = \phi_{\text{bep}}$  and  $\phi = 1.2\phi_{\text{bep}}$ ), and numerical data are compared with the PIV experiments. Fig. 12 presents the streamlines on the mid-span section of pump impeller obtained from the simulation and PIV test. The left column shows the numerical results, and the right column shows the results in the PIV test data for each operating condition. For the convenience of description of the rotating stall behavior, five blade-to-blade flow passages are marked A to E in Fig. 12.

Fig. 12(a) shows that a pair of vortices appear in four blade-to-blade flow passages at  $0.6\phi_{\text{bep}}$ , and the vortices near the blade suction side are larger than those near the pressure side. The strength or size of the vortex in one blade-to-blade passage is different from the others. The largest vortex is near the exit of blade-to-blade passage A, and the vortex near the entrance of the passage is also large enough to block the liquid flowing in blade-to-blade passage A. However, no vortex exists in blade-to-blade passage B. The numerical results generally reproduce the flow phenomena recorded in the PIV test. Based on the results shown in Fig. 6(a), the strong vortices in blade-to-blade passages A, E, D and C should induce rotating stall and result in the flow instability of the pump.

The numerical simulation at  $1.0\phi_{\text{bep}}$  may overestimate the vortex in the impeller compared with the PIV test, as shown in Fig. 12(b). In blade-to-blade passages A and B, the vortices are predicted by numerical simulation and have not been cap-

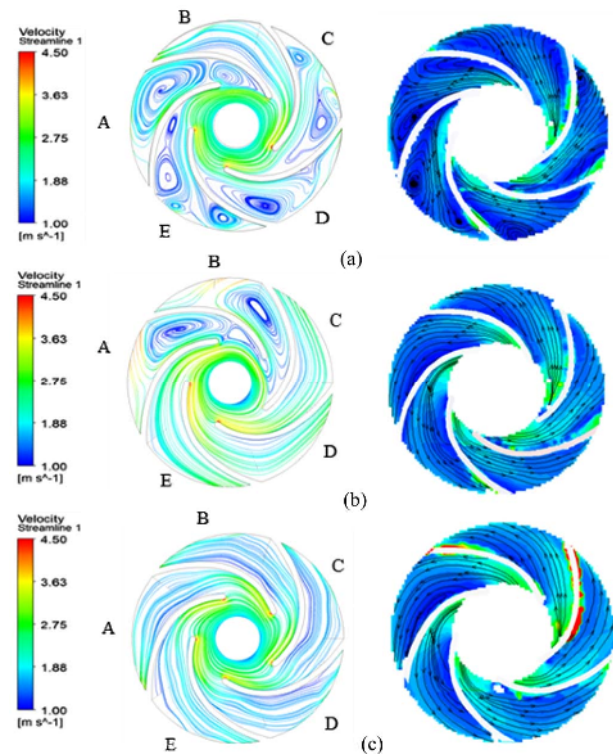


Fig. 12. Streamline comparisons between simulation and PIV tests at (a)  $0.6\phi_{\text{bep}}$ ; (b)  $\phi_{\text{bep}}$ ; (c)  $1.2\phi_{\text{bep}}$ .

tured in the PIV test. However, the tendency of flow separation near the blade pressure side can be observed from the PIV test results. The difference between the experiment and the simulation can be considered as the limitation of the  $k-\omega$  SST turbulence model. In the future, advanced turbulence models should be applied to investigate the flow instability phenomenon in centrifugal pumps.

In the case of  $1.2\phi_{\text{bep}}$ , the simulated streamlines, which are smooth, agree well with the experimental results shown in Fig. 12(c). No separation or vortex exists in all blade-to-blade passages, unlike under part-flow conditions. In addition, the energy loss in the impeller at this condition should be small.

##### 4.5.2 Evolution of stall cells

The timely dependent flow should be further investigated to depict the rotating stall in the impeller because vortex movement is strong at  $0.6\phi_{\text{bep}}$ . Fig. 13 illustrates the flow development at six instants in a rotation circle of the pump shaft, namely,  $t = 0, T/6, 2/6T, 3/6T, 4/6T$  and  $5/6T$ , where the parameter “ $T$ ” stands for the rotation period of the pump shaft. To better show this flow evolution, six images are shown in a rotation reference frame. At this operating condition, the vortex and its intensity change periodically in blade-to-blade passages A, E, D and C. Also, no remarkable vortex and relatively large velocity exist at any instant in blade-to-blade passage B during this period.

Blade-to-blade passage A is considered to analyze the un-

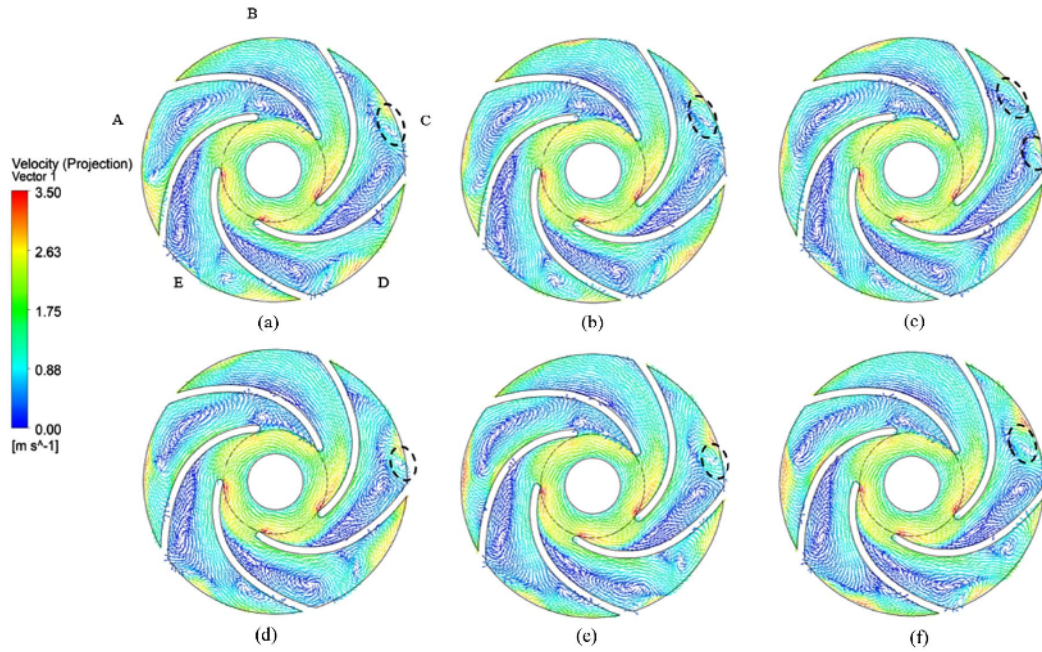


Fig. 13. Flow development at mid-span section of impeller at (a)  $t = 0$ ; (b)  $t = T/6$ ; (c)  $t = 2T/6$ ; (d)  $t = 3T/6$ ; (e)  $t = 4T/6$ ; (f)  $t = 5T/6$ .

steady flow phenomenon. At  $t = 0$ , a pair of vortices occur in the passage, whereby one occurs near the blade suction side and another occurs at the center of the passage. The vortex near the suction side almost blocks off the passage inlet, blocking the flow of fluid into the blade-to-blade passage. From  $t = T/6$  to  $t = 3T/6$ , the vortex oscillates near the inlet of the passage, and its intensity seems to decrease. From  $t = 4T/6$  to  $t = 5T/6$ , the inlet of the blade-to-blade passage is open along the blade suction side despite that flow blockage still exists near the pressure side. However, the corresponding area and intensity of the vortex located at the passage center remain nearly unchanged even though some oscillations can be observed during a shaft rotation period. A zone with high velocity magnitude exists at the impeller exit whose size changes at different instants, indicating the existence of flow oscillations.

Similar to blade-to-blade passage A, blade-to-blade passages E, D and C exhibit flow oscillations during one shaft rotation period. Blade-to-blade passage C has two vortices. The large one is along the suction side, and the small one is near the pressure side and the impeller exit, as shown at Fig. 13(a). At the instant of  $T/6$ , the vortex near the pressure side sheds off, and a new one forms due to the breakdown of the large vortex near the suction side, as shown in Fig. 13(b). A new vortex develops, shrinks, and moves toward the pressure side from  $t = 2T/6$  to  $t = 4T/6$ . At the instant of  $t = 5T/6$ , the vortex sheds off and a new vortex is formed, as shown in Fig. 13(f). Similar flow behaviors can be observed in blade-to-blade passages D and E.

To further capture the unsteady flow in the impeller at  $0.6\phi_{\text{bep}}$ , Fig. 14 presents the vorticity distribution at the mid-span section of the impeller in an evolution cycle of the rotat-

ing stall  $T_{\text{stall}}$ , which is recognized by vortex development in the blade-to-blade flow passages. The vortices at the impeller exit propagate along the direction of the shaft rotation. Consider the vortex marked with a circle in blade-to-blade passage C at  $t = 0$ . The vortex moves to blade-to-blade passage B at  $t = 2/12T_{\text{stall}}$ , blade-to-blade passage A at  $t = 4/12T_{\text{stall}}$ , blade-to-blade passage E at  $t = 6/12T_{\text{stall}}$ , and blade-to-blade passage D at  $t = 8/12T_{\text{stall}}$ . Moreover, the vortex at the impeller inlet in blade-to-blade A oscillates, and its intensity is largest at  $t = 2/12T_{\text{stall}}$  although the vortex seems to totally or partly block off the passage inlet in the entire circle. Note that the rotating stall in this impeller is much different from that in the guide vanes of a pump turbine [4], wherein the flow blockage and separated vortices rotate and shift from one passage to the next between two neighboring guide vanes. Furthermore, no strong vortex occurs and blocks off the flow at the inlet of the passage for blade-to-blade flow passage B. Thus, the blockage of blade-to-blade flow passage A and lack of blockage of blade-to-blade flow passage B are important features for the unsteady flow at part-load conditions. In this study, the evolution cycle of the rotating stall ( $T_{\text{stall}}$ ) is approximately 12 times the period of shaft rotation ( $T$ ).

The shed vortices will propagate downstream. Fig. 15 illustrates the flow at the middle section of the casing at  $0.6\phi_{\text{bep}}$  at a period of shaft rotation. The vortices oscillate near the casing outlet, whose position is indicated by a circle, as the flow changes in the impeller. During a rotation cycle of the impeller, the periodically changing vortices in the casing result in hydraulic loss and contribute to the flow instability in the pump.

The periodic development of the rotating stall in one evolution cycle can be divided into the stages of growth, mergence,



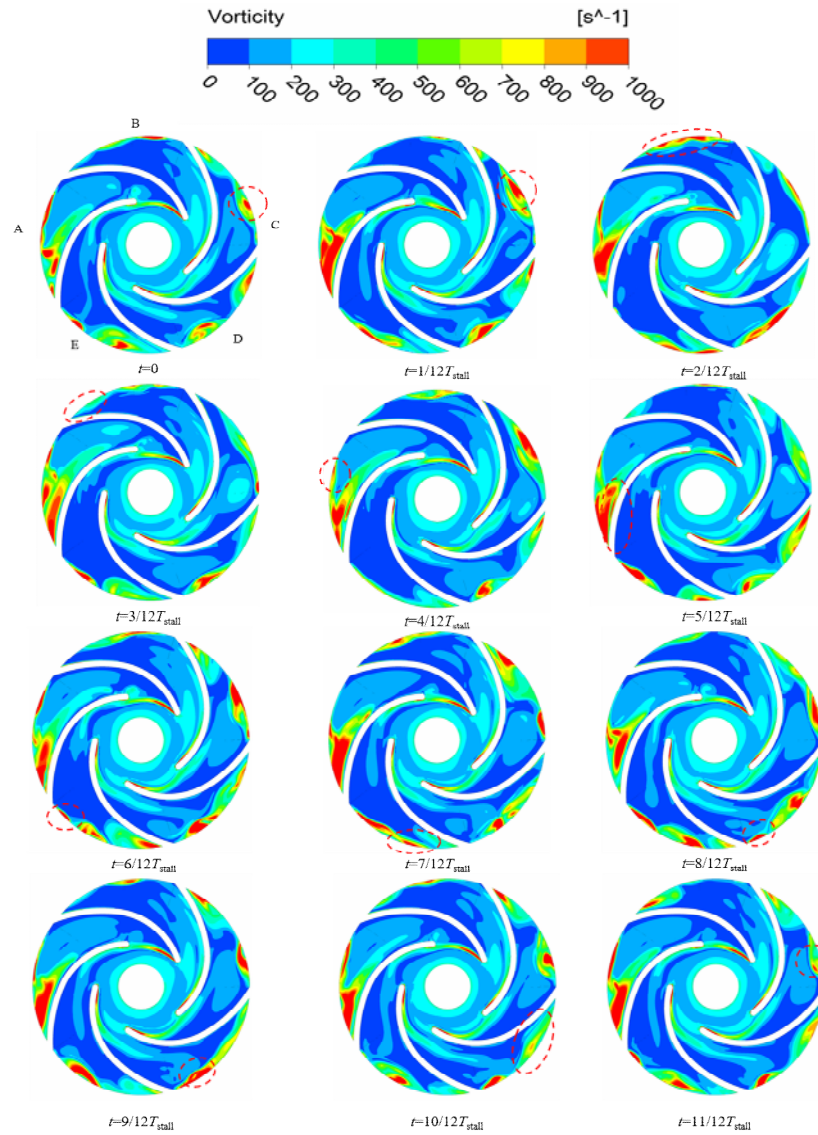


Fig. 14. Vorticity distribution at mid-span section of impeller in an evolution cycle of rotating stall.

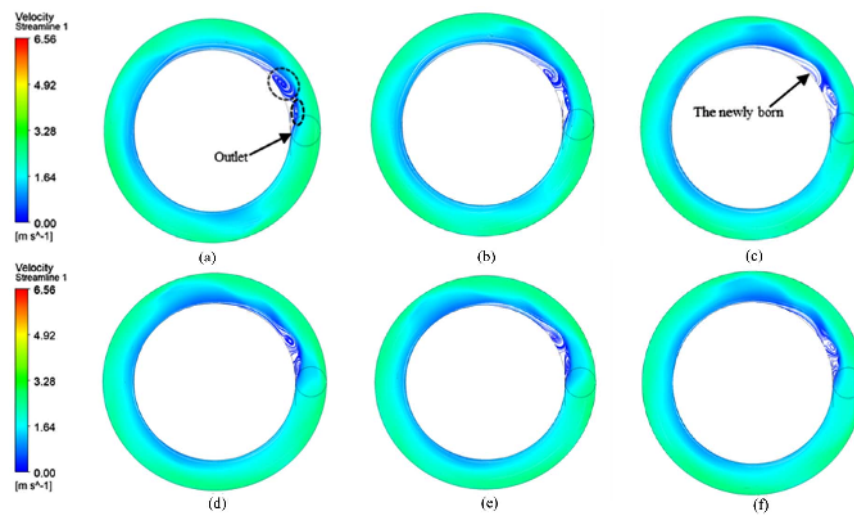


Fig. 15. Flow at middle section of casing at (a)  $t = 0$ ; (b)  $t = T/6$ ; (c)  $t = 2/6T$ ; (d)  $t = 3/6T$ ; (e)  $t = 4/6T$ ; (f)  $t = 5/6T$ .



development, split, decay, and shedding. The stall cells propagate at the same direction as the pump shaft rotation. However, the propagation speed of the rotating stall is much slower than the rotational speed of the pump shaft. The stall cells seem to rotate against the impeller. The periodic change and propagation of stall cells make the fluid redistribute in the passage and contribute to the flow instability. During this evolution cycle, the blockage coefficient [22] of the impeller flow passage changes periodically, and the blockage causes considerable energy loss and negatively affect the stability of pump operation.

The flow instability in the test pump is also affected by the special structure of the pump casing and that upstream the impeller. The effects of these structures on pump performance and the internal flow of the pump will be studied in the near future.

## 5. Conclusions

The flow instability phenomenon in a low-specific-speed centrifugal pump is investigated by using steady and unsteady flow simulation, and the flow inside the impeller is measured by PIV test. From the numerical and experimental results, the following conclusions can be drawn.

(1) The present numerical treatment is suitable for the simulation of flow instability in pumps. Regarding the performance prediction at part-load conditions, the accuracy of unsteady simulation is better than that of steady simulation.

(2) The energy loss in the impeller is the largest during special part-load conditions among all the flow components in the pump.

(3) During one revolution of the rotating stall, one blade-to-blade passage is always partially blocked off by the vortex occurring at the impeller inlet for each instant. The blockage of this blade-to-blade passage induces a jet flow with large velocity at the next blade-to-blade passage along the rotational direction of the impeller.

(4) The blockage and jet flow in the blade-to-blade passages will cause unstable flow in the impeller, performance breakdown, and pressure vibration.

## Acknowledgments

This work was financially supported by the National Natural Science Foundation of China (Grant No. 51536008), National Key R&D Program of China (2018YFB0606101), Beijing Natural Science Foundation (3182014), Science and Technology on Water Jet Propulsion Laboratory (Project No. 61422230103162223004), and State Key Laboratory for Hydroscience and Engineering (Project No. sklhse-2017-E-02).

## Nomenclature

$A$  : Section area ( $\text{m}^2$ )  
 $\text{bep}$  : Best efficiency point

$CP$  : Non-dimensional energy loss parameter  
 $D$  : Diameter (m)  
 $g$  : Gravitational acceleration  
 $H$  : Pump head (m)  
 $p$  : Pressure (Pa)  
 $P$  : Power (w)  
 $Q$  : Flow discharge ( $\text{m}^3/\text{h}$ )  
 $u$  : Velocity (m/s)  
 $\rho$  : Density ( $\text{kg}/\text{m}^3$ )

## References

- [1] J. Y. Mao, S. Q. Yuan, J. F. Zhang, Y. L. Li and Y. F. Wang, Analysis of inner flow characteristics in low specific speed centrifugal pump around hump conditions, *Journal of Drainage and Irrigation Machinery Engineering (JDIME)*, 33 (4) (2015) 283-289.
- [2] Y. X. Xiao, Y. Y. Yao, Z. W. Wang, J. Zhang, Y. Y. Luo, C. J. Zeng and W. Zhu, Hydrodynamic mechanism analysis of the pump hump district for a pump-turbine, *Engineering Computations*, 33 (3) (2016) 957-976.
- [3] Y. Ren, Z. C. Zhu, D. H. Wu, J. G. Mu and X. J. Li, An improved turbulence model for separation flow in a centrifugal pump, *Advances in Mechanical Engineering*, 8 (6) (2016) 1-10.
- [4] H. J. Ran, X. W. Luo, L. Zhu, Y. Zhang, X. Wang and H. Y. Xu, Experimental study of the pressure fluctuations in a pump turbine at large partial flow conditions, *Chinese Journal of Mechanical Engineering*, 25 (6) (2012) 1205-1209.
- [5] J. G. Mou, S. C. Zhang, S. H. Zheng and H. Y. Deng, Reason for centrifugal pump performance curve hump and the elimination method, *Transactions of the Chinese Society of Agricultural Machinery*, 37 (4) (2006) 56-59.
- [6] O. Braun, *Part-load flow in radial centrifugal pumps*, Lausanne: Ecole polytechnique f'ed'erale de Lausanne (Epfl) (2009).
- [7] G. Wuibaut, G. Bois, P. Dupont, G. Caignaert and M. Stanislas, PIV measurements in the impeller and the vaneless diffuser of a radial flow pump in design and off-design operating conditions, *Journal of Fluids Engineering*, 124 (3) (2002) 791-797.
- [8] A. Guedes, J. L. Kueny, G. D. Ciocan and F. Avellan, Unsteady rotor-stator analysis of hydraulic pump-turbine: CFD and experimental approach, *Proceedings of 21st IAHR Symposium on Hydraulic Machinery and Systems*, Lausanne, Sweden (2002).
- [9] M. Sinha, A. Pinarbasi and J. Katz, The flow structure during onset and developed states of rotating stall within a vaned diffuser of a centrifugal pump, *Journal of Fluids Engineering*, 123 (3) (2001) 490-499.
- [10] Y. Li, X. J. Li, Z. C. Zhu and F. Q. Li, Investigation of unsteady flow in a centrifugal pump at low flow rate, *Advances in Mechanical Engineering*, 8 (12) (2016) 1-8.
- [11] S. Bolpaire and J. P. Barrand, Experimental study of the flow in the suction pipe of a centrifugal pump at partial flow

- rates in unsteady conditions, *Journal of Pressure Vessel Technology*, 121 (3) (1999) 291-295.
- [12] C. Widmer, T. Staubli and N. Ledergerber, Unstable characteristics and rotating stall in turbine brake operation of pump-turbine, *Journal of Fluids Engineering*, 133 (4) (2011) 041101.
- [13] E. Outa, Rotating stall and stall-controlled performance of a single stage subsonic axial compressor, *Journal of Thermal Science*, 15 (1) (2006) 1-13.
- [14] S. Berten, P. Dupont, L. Fabre, M. Kayal, F. Avellan and M. Farhat, Experimental investigation of flow instabilities and rotating stall in a high energy centrifugal pump stage, *Proceedings of ASME 2009 Fluids Engineering Division Summer Meetings*, Vail, Colorado, USA (2009) 78562.
- [15] G. X. Gu, A. Sparks and S. S. Banda, An overview of rotating stall and surge control for axial flow compressors, *IEEE Transactions on Control Systems Technology*, 7 (6) (1999) 639-647.
- [16] G. D. Ciocan and J. L. Kueny, Experimental analysis of rotor-stator interaction in a pump-turbine, *Proceedings of 23th IAHR Symposium on Hydraulic Machinery and Systems*, Yokohama, Japan (2006) 216-226.
- [17] D. K. Walters and D. Cokljat, A three-equation eddy-viscosity model for Reynolds-averaged Navier-Stokes simulations of transitional flow, *Journal of Fluids Engineering*, 130 (12) (2008) 121401.
- [18] R. K. Byskov, C. B. Jacobsen and N. Pedersen, Flow in a centrifugal pump impeller at design and off-design conditions-Part II: Large Eddy simulations, *Journal of Fluids Engineering*, 125 (1) (2003) 73-83.
- [19] P. J. Zhou, F. J. Wang, Z. J. Yang and J. G. Mou, Investigation of rotating stall for a centrifugal pump impeller using various SGS models, *Journal of Hydrodynamics*, 29 (2) (2017) 235-242.
- [20] H. Le, P. Moin and J. Kim, Direct numerical simulation of turbulent flow over a backward-facing step, *Journal of Fluid Mechanics*, 330 (1) (1997) 349-374.
- [21] X. W. Luo, Y. Zhang, J. Q. Peng, H. Y. Xu and W. P. Yu, Impeller inlet geometry effect on performance improvement for centrifugal pumps, *Journal of Mechanical Science and Technology*, 22 (10) (2008) 1971-1976.
- [22] P. J. Zhou, F. J. Wang and J. G. Mou, Investigation of rotating stall characteristics in a centrifugal pump impeller at low flow rates, *Engineering Computations*, 34 (6) (2017) 1989-2000.



pump turbines.

**Weixiang Ye** obtained his Bachelor of Science degree from North China Electric Power University in 2017. He is currently a Ph.D. student at the Department of Energy and Power Engineering, Tsinghua University in Beijing, China. His main area of research is the flow instability phenomenon in pumps and



Power Engineering at Tsinghua University in Beijing, China.

**Xianwu Luo** obtained his Bachelor of Science and Master of Science degrees from Tsinghua University in Beijing, China, in 1991 and 1997, respectively, and his Ph.D. in mechanical engineering from Kyushu Institute of Technology, Japan, in 2004. He is currently a Professor at the Department of Energy and